

# **Supplementary Material to “Small-scale analysis of brittle-to-ductile transition behavior in pure tungsten”**

Yeonju Oh<sup>1</sup>, Won-Seok Ko<sup>2</sup>, Nojun Kwak<sup>1</sup>, Jae-il Jang<sup>3</sup>, Takahito Ohmura<sup>4,\*</sup>, and Heung Nam Han<sup>1,\*\*</sup>

<sup>1</sup> *Department of Materials Science and Engineering & Research Institute of Advanced Materials, Seoul National University, Seoul 08826, Republic of Korea*

<sup>2</sup> *School of Materials Science and Engineering, University of Ulsan, Ulsan 44610, Republic of Korea*

<sup>3</sup> *Division of Materials Science and Engineering, Hanyang University, Seoul, 04763, Republic of Korea*

<sup>4</sup> *National Institute for Materials Science, 1-2-1 Sengen, Tsukuba, Ibaraki 305-0047, Japan*

## Measurement of edge and screw dislocation density using XRD

In this study, we applied the modified Williamson–Hall (MWH) method to characterize the ratio of edge and screw components in a specimen using X-ray diffraction patterns. This method is based on the anisotropic contrast of dislocations in the diffraction pattern and is written as [1]:

$$\Delta K \cong 0.9/D + \left(\pi M^2 b^2 / 2\right)^{1/2} \rho^{1/2} K \sqrt{\bar{C}} \quad (\text{S1})$$

where  $\Delta K$ ,  $D$ ,  $\rho$ , and  $b$  are the peak width, average particle size, average dislocation density, and Burgers vector of dislocation, respectively.  $M$  is the dimensionless parameter depending on the effective outer cutoff radius of dislocation.  $K$  can be obtained using  $K=2\sin\theta/\lambda$ , where  $\theta$  and  $\lambda$  are the diffraction angle and wavelength, respectively.  $\bar{C}$  is the average contrast factor of dislocation that depends on  $\{hkl\}$  reflections. For the cubic structure,  $\bar{C}$  can be expressed as [2]:

$$\bar{C}_{hkl} = \bar{C}_{h00} (1 - qH^2) \quad (\text{S2})$$

$$H^2 = (h^2 k^2 + k^2 l^2 + l^2 h^2) / (h^2 + k^2 + l^2) \quad (\text{S3})$$

Here,  $\bar{C}_{h00}$  is the average dislocation contrast factor for  $\{h00\}$  reflections. The parameter  $q$  depends on the characteristic of dislocation (edge or screw) and can be experimentally determined [2]. The combination of Eq. (S1) with Eq. (S2) yields:

$$\left[ (\Delta K)^2 - \alpha \right] / K^2 \cong \beta \bar{C}_{h00} (1 - qH^2) \quad (\text{S4})$$

where  $\alpha = (0.9/D)^2$  and  $\beta = (\pi M^2 b^2 / 2) \rho$ . The intercept of the extrapolated line on the  $H^2$  axis, obtained via linear regression of Eq. (S4) with respect to  $H^2$ , provides the  $q$  parameter [3, 4]. The results of the linear regression for each specimen are shown in Fig. S1. If an equation for regression is expressed by  $y = Ax + B$ , the slope ( $A$ ) and  $y$ -axis intercept ( $B$ ) correspond to  $-q\beta\bar{C}_{h00}$  and  $\beta\bar{C}_{h00}$ , respectively. Subsequently,  $-A/B$  corresponds to the  $q$  value, as shown in Fig. S1. Once the  $q$  value is experimentally determined, each fraction of the edge and screw component can be estimated by comparing it with the corresponding theoretical  $q$  values ( $q^{\text{th}}$ ) of pure edge and screw components as follows [5]:

$$f_{edge} = \frac{q_{screw}^{th} - q}{q_{screw}^{th} - q_{edge}^{th}} \quad (S5)$$

Here,  $q^{th}$  for pure edge/screw dislocation can be determined using elastic anisotropy ( $A_n$ ), which is expressed by elastic constants ( $C_{11}$ ,  $C_{12}$ , and  $C_{44}$ ) as follows:

$$q^{th} = a^q [1 - \exp(\frac{-A_n}{b^q})] + c^q A_n + d^q \quad (S6)$$

$$A_n = \frac{2C_{44}}{C_{11} - C_{12}} \quad (S7)$$

where parameters  $a$ ,  $b$ ,  $c$ , and  $d$  also depend on the elastic constants of the materials.

$\bar{C}_{h00}$  is determined by a weighted average of  $C_{h00}$  values for pure edge and screw components considering the calculated fractions of each component.  $C_{h00}$  is also expressed by  $a$ ,  $b$ ,  $c$ , and  $d$  as follows [2]:

$$C_{h00} = a^c [1 - \exp(\frac{-A_n}{b^c})] + c^c A_n + d^c \quad (S8)$$

We have used the reported elastic constants,  $C_{11}$  (501 GPa),  $C_{12}$  (198 GPa), and  $C_{44}$  (151 GPa), of pure W [6]. Other parameters required for Eqs. (S6) and (S8) are listed in Table S1 [2].

$\bar{C}_{h00}$  values of each specimen obtained using Eq. S8 were further used in the CMWP analysis to calculate the total dislocation density. The input values for the CMWP fitting including the obtained  $\bar{C}_{h00}$  values of each specimen are listed in Table S2.

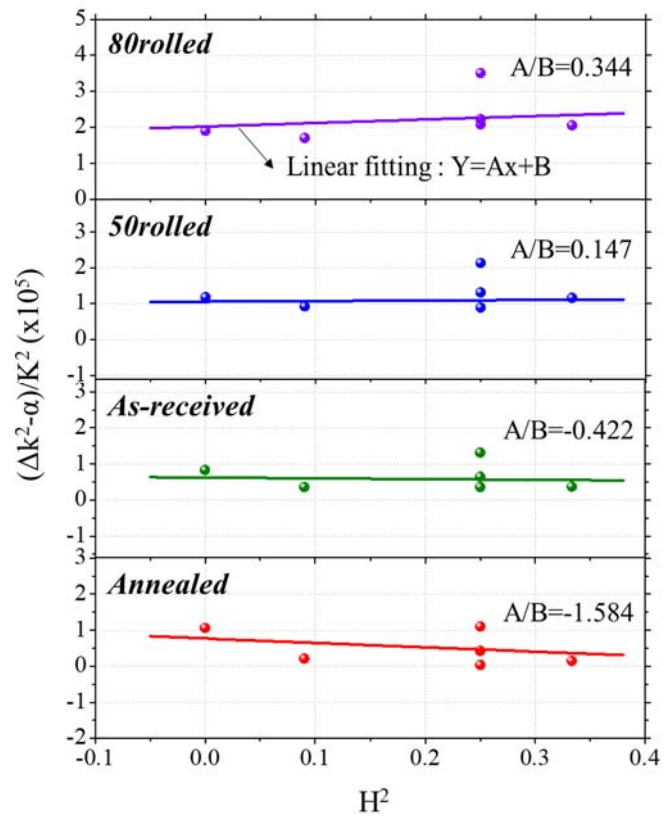


Figure S1 Input values (points) and results (lines) of linear regressions of each specimen based on Eq. (S4). The slope ( $A$ ) and y-axis intercept ( $B$ ) of the optimized linear equation were used to obtain the  $q$  parameter ( $-A/B$ ).

Table S1 Input values of the parameters ( $a$ ,  $b$ ,  $c$ , and  $d$ ) of Eqs. S6 and S8 for determining  $q$  and  $C_{h00}$  for the pure screw and edge components [2].

Parameter	Screw	Edge
$a^q$	8.6590	7.2361
$b^q$	0.3730	0.9285
$c^q$	0.0424	0.1359
$d^q$	-6.074	-5.7484
$a^C$	0.1740	1.6690
$b^C$	1.9522	21.124
$c^C$	0.0293	0
$d^C$	0.0662	0.0757

Table S2 Input values of the parameters used in the CMWP fitting to obtain the total dislocation density.

Specimen	Lattice parameter (Å)	Burgers vector, (nm)	$\bar{C}_{h00}$
80rolled			0.155
50rolled			0.156
As-received	3.159 <sup>a</sup>	0.274 <sup>a</sup>	0.158
Annealed			0.163

<sup>a</sup> Ref. [6]

### *Development of the 2NN MEAM interatomic potential for pure W*

In the 2NN MEAM potential formalism, 14 independent parameters are necessary to describe a pure element. Four of these parameters [the cohesive energy ( $E_c$ ), the equilibrium nearest-neighbor distance ( $r_e$ ), the bulk modulus ( $B$ ) of the reference structure and the adjustable parameter ( $d$ )] are related to the universal equation of state. Seven further parameters [the decay lengths ( $\beta^{(0)}$ ,  $\beta^{(1)}$ ,  $\beta^{(2)}$ ,  $\beta^{(3)}$ ) and weighting factors ( $t^{(1)}$ ,  $t^{(2)}$ ,  $t^{(3)}$ )] are related to the electron density. The parameter  $A$  belongs to the embedding function and the parameters  $C_{\min}$  and  $C_{\max}$  are responsible for the many-body screening. Details for the unary parameters are given in Refs. [7, 8].

We developed the 2NN MEAM interatomic potential for pure W based on the force-matching method proposed by Ercolessi and Adams [9]. We followed a previously published procedure [10] in which 2NN MEAM potentials for pure Ni and Ti systems were determined. First, we performed DFT calculations for various atomic configurations to construct a database of atomic energies and forces. Configurations resulting from various temperature, strain and defect conditions were included in the database to assure the sufficient transferability of the potential to variety of applications. We then optimized the potential parameters by minimizing errors between energies and forces expected by DFT calculations and those expected by temporary potential parameters. The bcc structure was selected as a reference structure and experimentally reported cohesive energy of the bcc W (8.66 eV [11]) was used as the  $E_c$  value. Table S3 presents the finally determined potential parameters for pure W. In atomistic simulations, the selection of an optimum radial cutoff distance, considering the accuracy and computational cost, is indispensable. In this study, we selected comparably large radial cutoff (6.0 Å) and truncation (2.0 Å) distances in all atomistic simulations to avoid possible artifacts caused by abnormally large bond-breaking forces [12].

Table S3 2NN MEAM potential parameter sets for pure W system. The following properties are dimensionful: the cohesive energy  $E_c$  (eV/atom), the equilibrium nearest-neighbor distance  $r_e$  (Å), and the bulk modulus  $B$  ( $10^{12}$  dyne/cm<sup>2</sup>). The reference structure is bcc W.

	$E_c$	$r_e$	$B$	$A$	$\beta^{(0)}$	$\beta^{(1)}$	$\beta^{(2)}$	$\beta^{(3)}$	$t^{(1)}$	$t^{(2)}$	$t^{(3)}$	$C_{\min}$	$C_{\max}$	$d$
Present	8.66	2.74	0.3124	3.033	7.19	0.00	0.98	2.70	-3.00	-4.96	-10.23	0.41	2.60	0.03
Lee <sup>a</sup>	8.66	2.74	3.1418	0.40	6.54	1.00	1.00	1.00	-0.60	0.30	-8.70	0.49	2.80	0.00

<sup>a</sup> Ref. [7]

### ***Accuracy and transferability of developed interatomic potential for pure W***

The accuracy and transferability of the developed 2NN MEAM potential were evaluated by comparing the results for various physical properties to the experimental and DFT computed values. If not designated as MD simulations, the calculated properties represent the results of molecular statics simulations at 0 K using supercells with at least 4000 atoms allowing for full relaxation of cell dimensions and individual atomic positions. Periodic boundary conditions were applied along all three dimensions, except for the calculation of surface energies.

We evaluated the accuracy of the pure W potential by investigating the physical properties that are closely related to the atomic configurations of the DFT database used for parameter optimization. In Table S4, the bulk, elastic, and defect properties at 0 K are compared with experimental data, DFT calculations, and the previous potential by [7]. The experimental cohesive energy of the bcc phase is precisely reproduced because the optimization was performed using this value. The lattice constant, elastic constants, and properties related to the vacancy ( $E_f^{\text{vac}}$ ,  $E_m^{\text{vac}}$ ,  $Q^{\text{vac}}$ ) are satisfactorily reproduced. Generally, the accuracy of the developed potential and previous potential [7] in reproducing the aforementioned properties is satisfactory. However, the previous potential [7] shows significant discrepancies in reproducing the structural energy differences and surface energy.

The remaining properties for the comparison are those that are not used directly during the optimization. We can evaluate the transferability of the developed potential by investigating these properties. Figure S2 shows the phonon dispersion relation of bcc W for the present and previous potential [7], in comparison with the present DFT calculations and experiments [13]. The previous potential [7] shows an underestimation of the DFT frequencies, especially at the  $H$  point. The present potential reproduces the overall dependence of the phonon branches in a better agreement with the DFT and experimental data. For the thermal expansion coefficient and specific heat shown in Fig. S3, the present potential and the previous potential [7] exhibit no clear difference in the reproducibility of the experiment.

The transferability of the present potential was further examined by comparing thermal properties such as the expansion coefficient, heat capacity, melting temperature, melting enthalpy, and volume change upon melting. These properties were evaluated using MD simulations in an isobaric-isothermal ( $NPT$ ) ensemble. The melting temperature was calculated using the interface method, which employs a cell consisting of a liquid and solid phase at zero

pressure. The enthalpy of melting and volume change upon melting were calculated using the obtained melting temperature at zero pressure. Table S5 illustrates the calculated thermal properties compared with the experimental data. The developed potential generally shows better results compared to the previous potential [7]. The improvement is particularly significant in reproducing the melting temperature ( $T_m$ ). This can be explained by the present optimization procedure, which includes atomic configurations of the liquid phase in the fitting database, while the previous optimization by Ref. [7] did not focus on the liquid phase.

Table S4 Calculated bulk and defect properties of pure W using the present 2NN MEAM potential, in comparison with experimental data, DFT data, and previous 2NN MEAM calculations by [7]. The following quantities are listed: the cohesive energy  $E_c$  (eV/atom), the lattice constant  $a$  (Å), the bulk modulus  $B$  and the elastic constants  $C_{11}$ ,  $C_{12}$ , and  $C_{44}$  ( $10^{12}$  dyne/cm<sup>2</sup>), the structural energy differences  $\Delta E$  (eV/atom), the vacancy formation energy  $E_f^{\text{vac}}$  (eV), the vacancy migration energy  $E_m^{\text{vac}}$  (eV), the activation energy of vacancy diffusion  $Q^{\text{vac}}$  (eV), and the surface energies  $E_{\text{surf}}$  (erg/cm<sup>2</sup>) for the orientations (indicated by the superscript).

Property	Exp.	DFT <sup>i</sup>	2NN MEAM Ref. [7]	2NN MEAM [Present study]
$E_c$	8.660 <sup>a</sup>	8.394	8.660	8.660
$a$	3.164 <sup>b</sup>	3.185	3.164	3.164
$B$	3.141 <sup>c</sup>	3.040	3.141	3.123
$C_{11}$	5.326 <sup>c</sup>	5.096	5.326	5.501
$C_{12}$	2.050 <sup>c</sup>	2.074	2.050	1.936
$C_{44}$	1.631 <sup>c</sup>	1.325	1.631	1.468
$\Delta E_{\text{bcc} \rightarrow \text{fcc}}$		0.485	0.263	0.402
$\Delta E_{\text{bcc} \rightarrow \text{hcp}}$		- <sup>j</sup>	0.215	0.363
$E_f^{\text{vac}}$	3.6 <sup>d</sup>	3.34	3.95	3.937
$E_m^{\text{vac}}$		1.64		1.472
$Q^{\text{vac}}$	5.4 <sup>e</sup>	4.98	5.56	5.409
$E_{\text{surf}}^{(100)}$	2990 <sup>f,h</sup> , 3468 <sup>g,h</sup>	4000	3900	3877
$E_{\text{surf}}^{(110)}$	2990 <sup>f,h</sup> , 3468 <sup>g,h</sup>	3228	3427	3090
$E_{\text{surf}}^{(111)}$	2990 <sup>f,h</sup> , 3468 <sup>g,h</sup>	3510	4341	3986

<sup>a</sup> Ref. [14]

<sup>b</sup> Ref. [15]

<sup>c</sup> Ref. [16]

<sup>d</sup> Ref. [17]

<sup>e</sup> Ref. [18]

<sup>f</sup> Ref. [19]

<sup>g</sup> Ref. [20]

<sup>h</sup> The experimental value is for a polycrystalline solid.

<sup>i</sup> Present DFT calculations.

<sup>j</sup> The hcp structure is unstable.

Table S5 Calculated thermal properties of pure W using the present 2NN MEAM potential, in comparison with experimental data and previous 2NN MEAM calculations by Ref. [7]. The listed quantities correspond to the thermal expansion coefficient  $\varepsilon$  ( $10^{-6}/\text{K}$ ), heat capacity at constant pressure  $C_p$  (J/mol K), melting temperature  $T_m$  (K), enthalpy of melting  $\Delta H_m$  (kJ/mol), and volume change upon melting  $\Delta V_m/V_{\text{solid}}$  (%).

Property	Exp. <sup>a</sup>	2NN MEAM Ref. [7]	2NN MEAM [Present study]
$\varepsilon$ (0–100 °C)	4.5 <sup>a</sup>	4.2	4.63
$C_p$ (0–100 °C)	25.4 <sup>a</sup>	25.4	25.4
$T_m$	3695 <sup>b</sup>	4600	3915
$\Delta H_m$	52.3 <sup>b</sup>	33.0	29.7
$\Delta V_m/V_{\text{solid}}$		3.2	3.46

<sup>a</sup> Ref. [21]                      <sup>b</sup> Ref. [22]

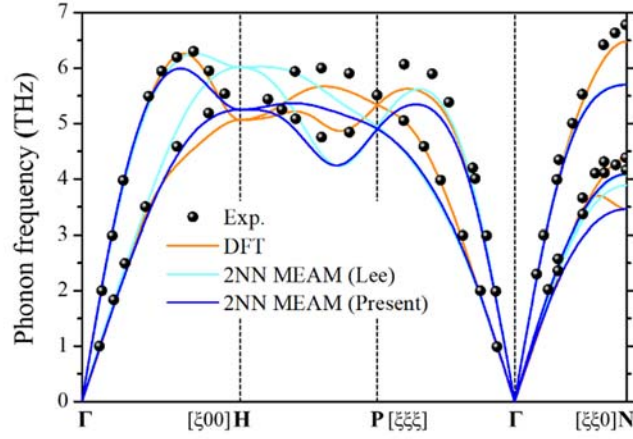


Figure S2 Calculated phonon spectra of bcc W using the present 2NN MEAM potential, in comparison with the experimental data [13], DFT results, and previous calculations by Ref. [7].

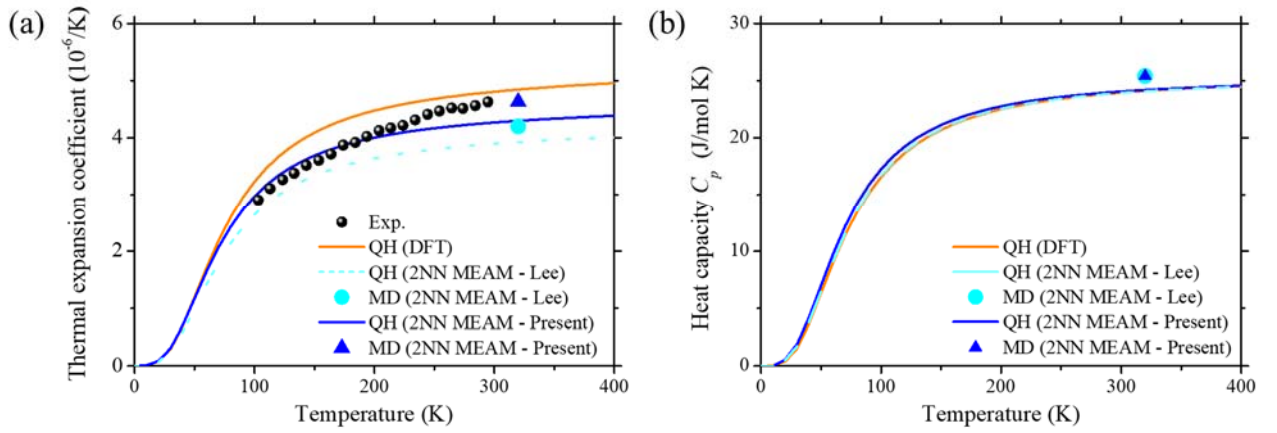


Figure S3 (a) Thermal expansion coefficients and (b) heat capacity of bcc W calculated based on the quasi-harmonic (QH) approximation and full MD simulations, in comparison with experimental data [23], DFT results, and previous calculations by Ref. [7].

### ***Analytical solution of thermally activated pop-in phenomenon***

During the nanoindentation, pop-in is detected as a sudden excursion in load-displacement curves, which is regarded as thermally activated process. Eq. (4) in the manuscript indicates the local rate at which the first displacement burst would occur per a unit volume under a specific stress state. For clearer description, the Eq. (4) can be separated into individual components as follows [24],

$$\dot{n} = \eta \exp\left(-\frac{Q}{kT}\right) \exp\left(\frac{\tau_{\max} V^*}{kT}\right) \quad (\text{S9})$$

where the first exponential term gives the probability per attempt of a pop-in event in a perfect, stress-free crystal, and the second makes explicit the exponential dependence of the rate of displacement bursts due to the action of a shear stress,  $\tau_{\max}$ .

For a series of nominally identical indentations such as in our experiments, the cumulative fraction function,  $F(t)$ , for the statistics of the first burst can be derived as follows [24].

$$F(t) = 1 - \exp\left(-\int_0^t \dot{N}(t') dt'\right) \quad (\text{S10})$$

$$\dot{N} = \eta \exp\left(-\frac{Q}{kT}\right) \cdot \iiint_{\Omega} \exp\left(\frac{\tau_{\max} V^*}{kT}\right) d\Omega \quad (\text{S11})$$

Here,  $\Omega = K\left(\frac{3p\rho}{4E_r}\right)$  according to the Hertzian theory where K is a proportionality constant taken to be of order  $\sim\pi$ . Considering  $P = \dot{P}t$  by the experimental condition with constant loading rate, and the definition of  $\tau_{\max}$  (Eq. (3) in manuscript),  $F(t)$  can be readily converted to cumulative load statistics as Eq. (5) in manuscript. The Eq. (5) can be lineally rewritten in a form that isolates Q,

$$P^{1/3} = \gamma kT + \frac{Q}{\psi V^*} \quad (\text{S12})$$

$$\gamma = \ln \left\{ \ln \left( \frac{1}{1-F(P_p)} \right) \left[ \frac{4E_r \dot{P}_p \alpha^6}{9KR\eta (120 \exp(-P_p^{1/3} \alpha) + P_p^{5/3} \alpha^5 - 5P_p^{4/3} \alpha^4 + 20P_p \alpha^3 - 60P_p^{2/3} \alpha^2 + 120P_p^{1/3} \alpha - 120)} \right] \right\} / \psi V^* \quad (\text{S13})$$

$$\psi = \frac{0.47}{\pi} \left( \frac{4E_r}{3R} \right)^{2/3} \quad (\text{S14})$$

Given the definition of  $\tau_{max} = \Psi P^{1/3}$  as Eq. (3), Eq. (S14) can be finally converted to Eq.

(7) in manuscript. Here,  $\gamma_p'$  in Eq. (7) is

$$\gamma_p' = \ln \left\{ \ln \left( \frac{1}{1-F(P_p)} \right) \left[ \frac{4E_r \dot{P}_p \alpha^6}{9KR\eta (120 \exp(-P_p^{1/3} \alpha) + P_p^{5/3} \alpha^5 - 5P_p^{4/3} \alpha^4 + 20P_p \alpha^3 - 60P_p^{2/3} \alpha^2 + 120P_p^{1/3} \alpha - 120)} \right] \right\} / V^* \quad (\text{S15})$$

Supplementary figures

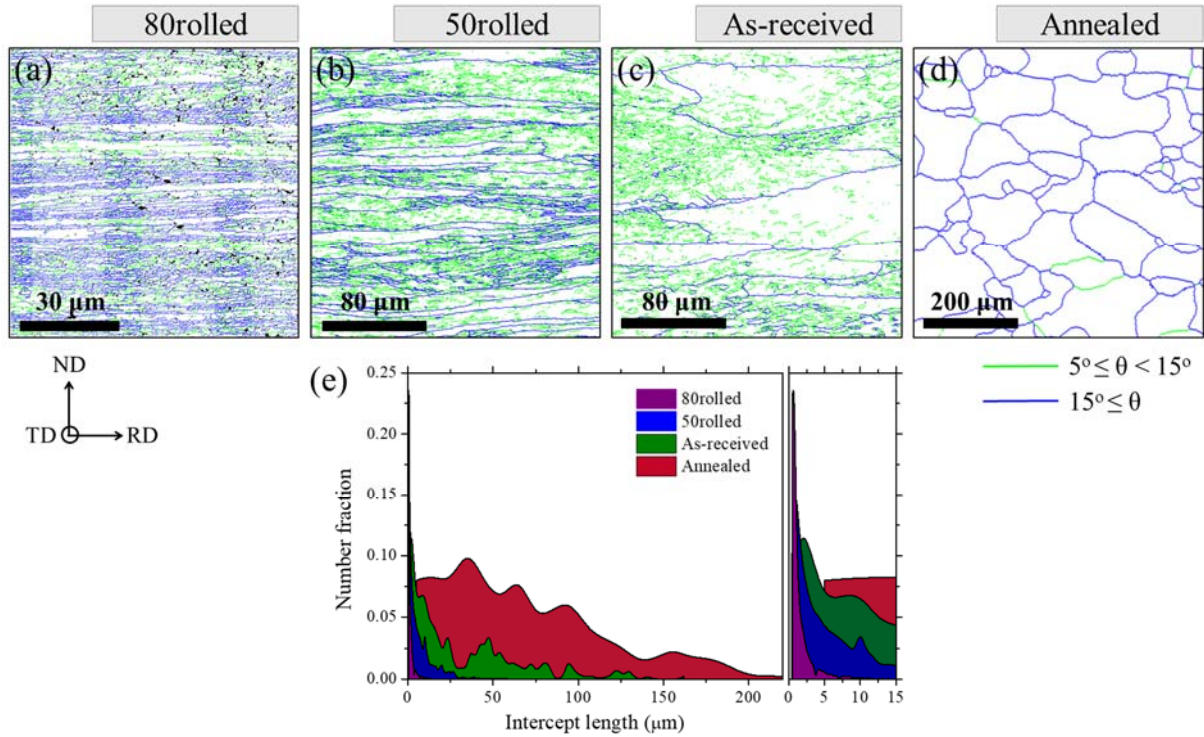


Figure S4 Representative grain boundary (GB) maps visualized along the TD of (a) 80rolled, (b) 50rolled (c) as-received, and (d) annealed specimens used to identify the GBs and grain morphologies. High-angle ( $15^\circ \leq \theta$ ) and low-angle ( $5^\circ \leq \theta < 15^\circ$ ) GBs are depicted using blue and green colors, respectively. The average grain size of each specimen was determined according to the line intercept method using GBs maps along the RD and TD. (e) Distribution of measured grain sizes of each specimen, which is determined by the line intercept method with a tolerance angle of  $15^\circ$ .

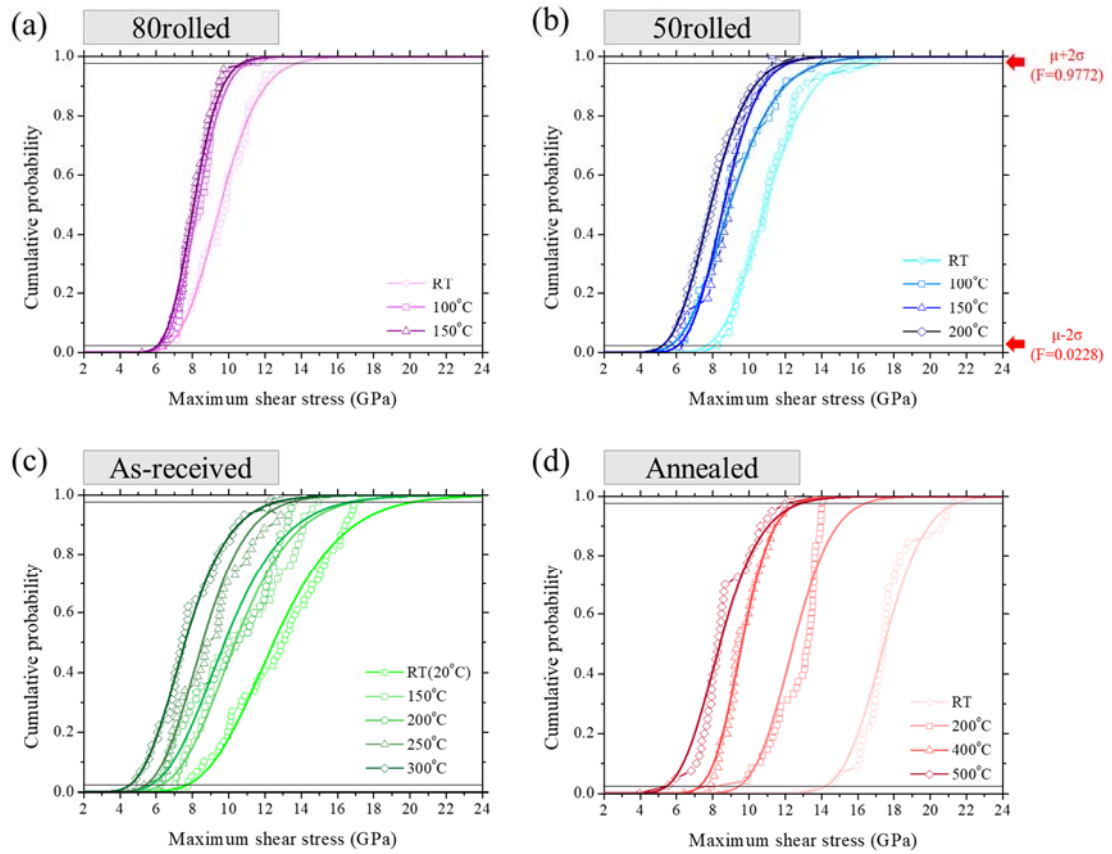


Figure S5 Cumulative probabilities for the maximum shear stress [ $F(\tau_{max})$ ] of (a) 80rolled, (b) 50rolled, (c) as-received, and (d) annealed specimens. Experimental data and the fitted cumulative functions of the lognormal distribution are represented by empty symbols and solid lines, respectively.  $\mu$  and  $\sigma$  indicate the mean and standard deviation determined using the lognormal distribution fitting. Here, the interval of  $\mu \pm 2\sigma$  corresponds to the interval between 2.28% [ $F(\tau_{max}) = 0.0228$ ] and 97.72% [ $F(\tau_{max}) = 0.9772$ ].

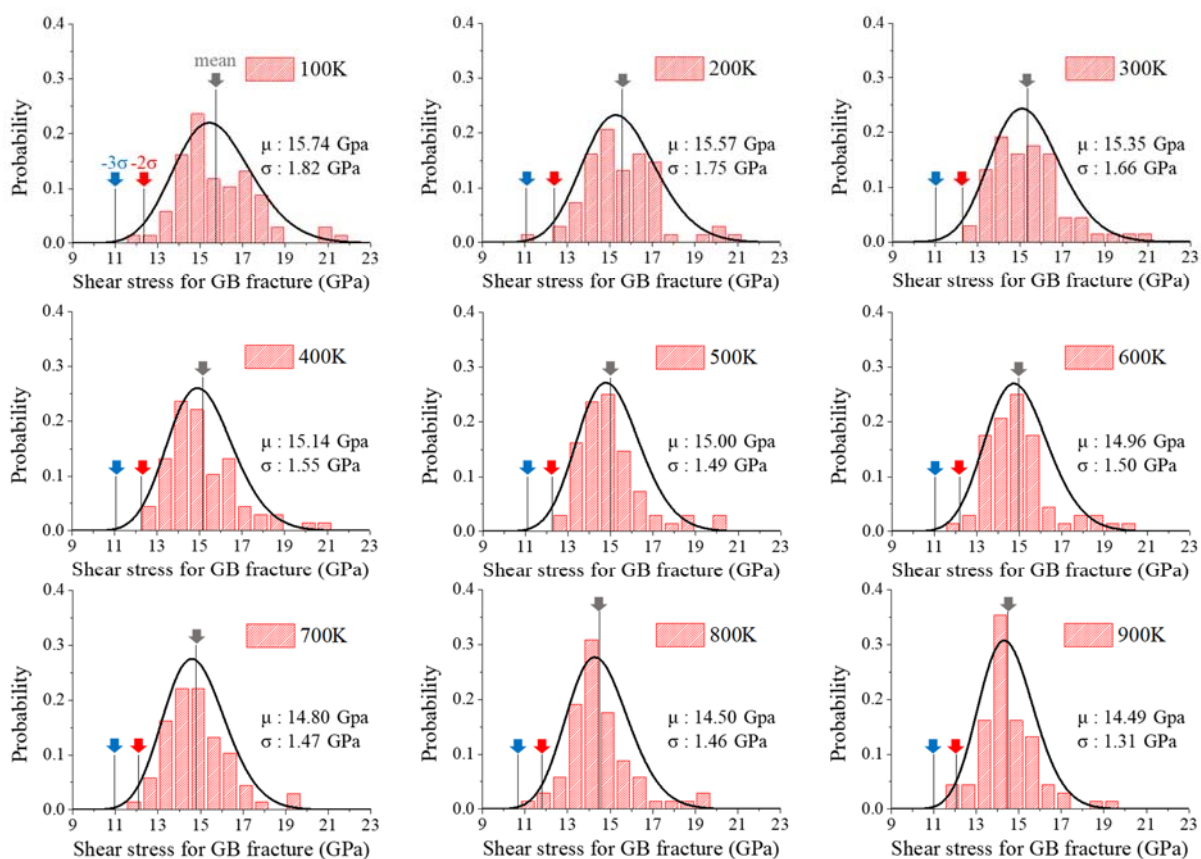


Figure S6 Distribution of GB fracture shear stress (red bar) with lognormal distribution fitting (black line) at various temperatures. The mean value ( $\mu$ ) and standard deviation ( $\sigma$ ) of the lognormal distribution are indicated. Each distribution contains the full dataset considered in the present work. Values corresponding to  $\mu$ ,  $(\mu-2\sigma)$ , and  $(\mu-3\sigma)$  are indicated by grey, red, and blue arrows, respectively.

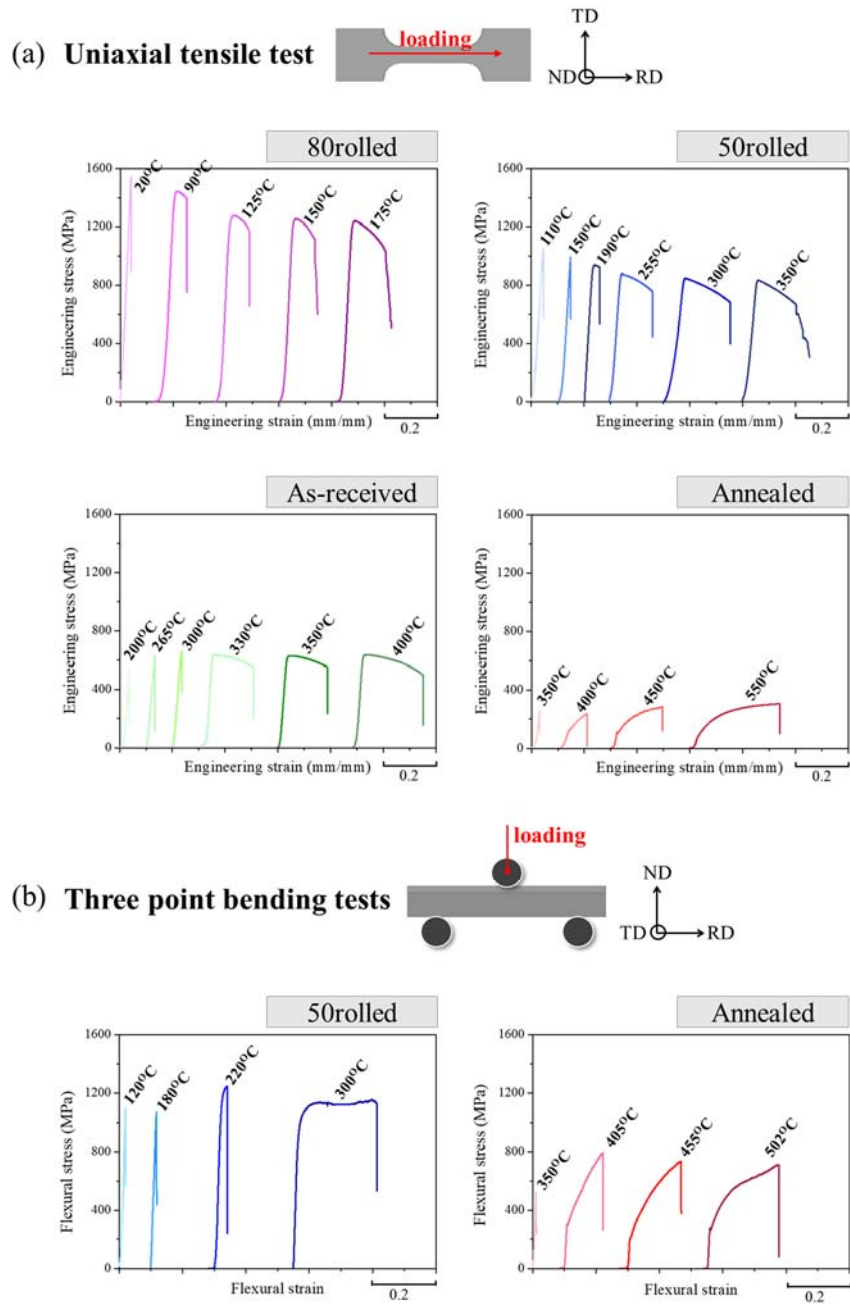


Figure S7 (a) Typical engineering stress–strain curves resulting from uniaxial tensile tests at various temperatures. (b) Flexural stress-strain responses in three point bending tests at various temperatures. The specimen orientation and the loading direction are represented by schematic, respectively.

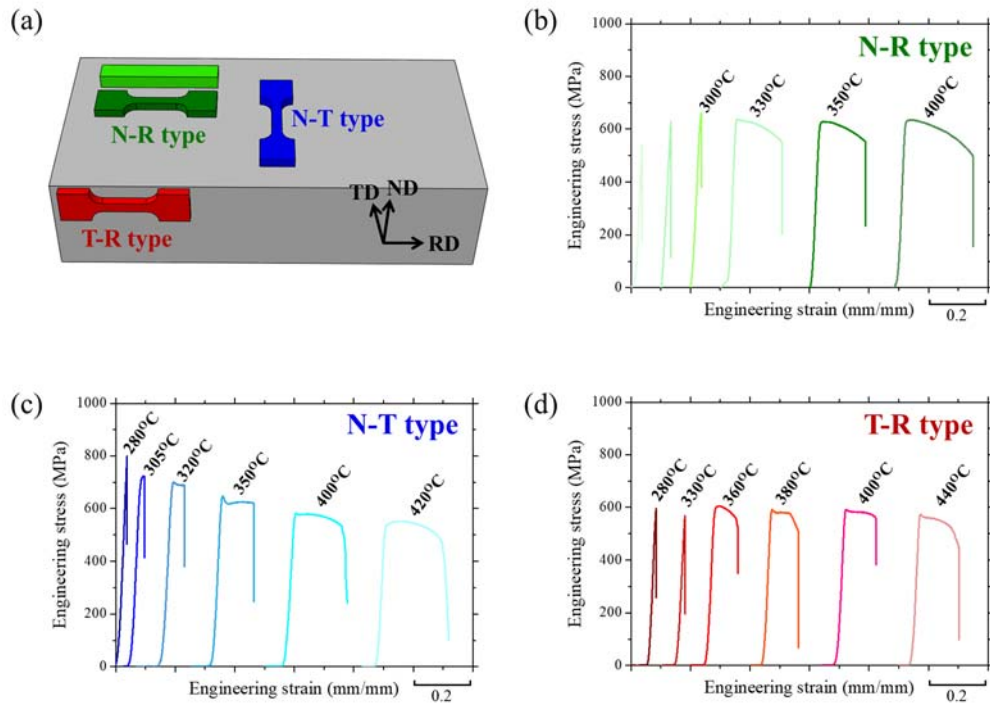


Figure S8 (a) Schematic representation of specimens extracted from the as-received rolled plate with different orientation. Typical engineering stress–strain curves resulting from uniaxial tensile tests at various temperatures with the specimen type of (b) N-R type, (c) N-T type, and (d) T-R type.

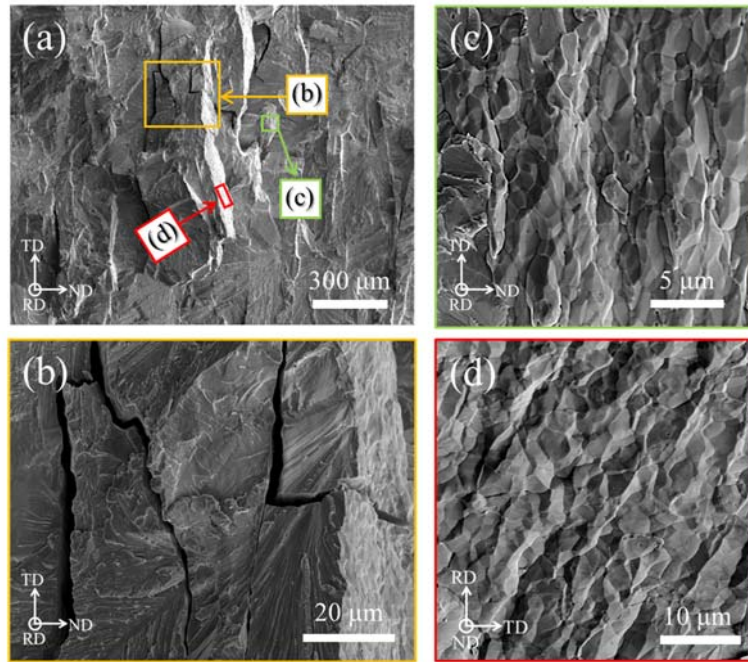


Figure S9 Fractographs of as-received specimen after tensile loading along RD at 300 °C, showing a totally brittle fracture. (a) Overview of the fracture surface in RD plane, where both of intergranular and cleavage fractures are observed simultaneously. (b) Magnified image marked in (a) with an orange-colored box, showing large and small cracks propagating along the grain boundaries of the elongated grains along TD (c) Magnified image marked in (a) with a green-colored box, showing the intergranular fracture appearances along the low-angle grain boundaries. (d) Magnified image marked in (a) observed along ND with a red-colored box, in which all fracture modes were definitely intergranular fracture, indicating that the cracks in the direction of loading rapidly propagated along the elongated grain boundaries.

### ***References for supplementary material***

- [1] T. Ungár, A. Borbély, The effect of dislocation contrast on x-ray line broadening: a new approach to line profile analysis, *Appl. Phys. Lett.*, 69 (1996) 3173-3175.
- [2] T. Ungár, I. Dragomir, Á. Révész, A. Borbély, The contrast factors of dislocations in cubic crystals: the dislocation model of strain anisotropy in practice, *J. Appl. Crystallogr.*, 32 (1999) 992-1002.
- [3] F. HajyAkbari, J. Sietsma, A.J. Böttger, M.J. Santofimia, An improved X-ray diffraction analysis method to characterize dislocation density in lath martensitic structures, *Mater. Sci. Eng., A*, 639 (2015) 208-218.
- [4] E. Schafner, M. Zehetbauer, T. Ungar, Measurement of screw and edge dislocation density by means of X-ray Bragg profile analysis, *Mater. Sci. Eng., A*, 319 (2001) 220-223.
- [5] Z. Cong, Y. Murata, Dislocation Density of Lath Martensite in 10Cr-5W Heat-Resistant Steels, *Mater. Trans., JIM*, 52 (2011) 2151-2154.
- [6] E. Lassner, W. Schubert, *Tungsten: Properties, Chemistry, Technology of the Element, Alloys, and Chemical Compounds*, Kluwer Academic/Plenum Publishers. xix, New York, 1999.
- [7] B.-J. Lee, M.I. Baskes, H. Kim, Y.K. Cho, Second nearest-neighbor modified embedded atom method potentials for bcc transition metals, *Phys. Rev. B: Condens. Matter*, 64 (2001) 184102.
- [8] B.-J. Lee, W.-S. Ko, H.-K. Kim, E.-H. Kim, The modified embedded-atom method interatomic potentials and recent progress in atomistic simulations, *Calphad*, 34 (2010) 510-522.
- [9] F. Ercolessi, J.B. Adams, Interatomic Potentials from First-Principles Calculations: The Force-Matching Method, *Europhys. Lett.*, 26 (1994) 583.
- [10] W.-S. Ko, B. Grabowski, J. Neugebauer, Development and application of a Ni-Ti interatomic potential with high predictive accuracy of the martensitic phase transition, *Phys. Rev. B: Condens. Matter*, 92 (2015).
- [11] C. Kittel, *Introduction to Solid State Physics*, 8th ed., Wiley, New York, 2005.
- [12] W.-S. Ko, B.-J. Lee, Origin of unrealistic blunting during atomistic fracture simulations based on MEAM potentials, *Philos. Mag.*, 94 (2014) 1745-1753.
- [13] S.H. Chen, B.N. Brockhouse, Lattice vibrations of tungsten, *Solid State Commun.*, 2 (1964) 73-77.
- [14] C. Kittel, *Introduction to solid state physics*, 8th ed., Wiley New York, 2005.

- [15] J.S. Shah, M.E. Straumanis, Thermal Expansion of Tungsten at Low Temperatures, *J. Apply. Phys.*, 42 (1971) 3288-3289.
- [16] G. Simmons, H. Wang, *Single Crystal Elastic Constants and Calculated Aggregate Properties: A Handbook*, 2nd ed., MIT Press, Cambridge, 1971.
- [17] H. Schultz, *Landolt–Börnstein New Series, Group III*, in, Springer, Berlin, 1991.
- [18] R.W. Siegel, *Proc. Yamada Conf. on Point Defects and Defect Interactions in Metals*, in, University of Tokyo Press, Tokyo, 1982, pp. 533.
- [19] W.R. Tyson, W.A. Miller, Surface free energies of solid metals: Estimation from liquid surface tension measurements, *Surf. Sci.*, 62 (1977) 267-276.
- [20] L.Z. Mezey, J. Giber, The Surface Free Energies of Solid Chemical Elements: Calculation from Internal Free Enthalpies of Atomization, *Jpn. J. Apply. Phys*, 21(Part 1, No. 11) (1982) 1569-1571.
- [21] E.A. Brandes, G.B. Brook, *Smithells Metals Reference Book*, 7th ed., in, Butterworth-Heinemann, Oxford, 1992.
- [22] A.T. Dinsdale, SGTE data for pure elements, *Calphad*, 15(4) (1991) 317-425.
- [23] F.C. Nix, D. MacNair, The Thermal Expansion of Pure Metals. II: Molybdenum, Palladium, Silver, Tantalum, Tungsten, Platinum, and Lead, *Phys. Rev.*, 61 (1942) 74-78.
- [24] J. Mason, A. Lund, C. Schuh, Determining the activation energy and volume for the onset of plasticity during nanoindentation, *Phys. Rev. B: Condens. Matter*, 73 (2006) 054102.